Supporting Information

Local nanostructures enhanced thermoelectric performance of n-type PbTe

Bo Xiang[#], Jiaqin Liu[#,] Jian Yan[*], Minggang Xia, Qi Zhang, Lingxue Chen, Jiayong Li, Xian Yi Tan, Qingyu Yan[*], Yucheng Wu[*]

Mr. B. Xiang, Prof. J. Q. Liu, Prof. J. Yan, Dr. Q. Zhang, Mr. L. X. Chen, Mr. J. Y. Li, Prof. Y. C. Wu
School of Materials Science and Engineering and Institute of Industry & Equipment Technology, Hefei University of Technology, Hefei, 230009, China.
Key Laboratory of Advanced Functional Materials and Devices of Anhui Province, Hefei 230009, China
Mr.X. Y. Tan, Prof Q. Y. Yan
School of Materials Science and Engineering, Nanyang Technological University, 50 Nanyang Avenue Blk N4.1 Singapore 639798.
Prof. M. G. Xia
Department of Photoelectronic Information Science Technology and Engineering, School of Science, Xi'an Jiaotong University, 710049, People's Republic of China.
E-mail: yanjian@hfut.edu.cn alexyan@ntu.edu.sg, ycwu@hfut.edu.cn

Keywords: local nanostructure, PbTe, Ag dynamic doping, structure controlling, diffusion barrier
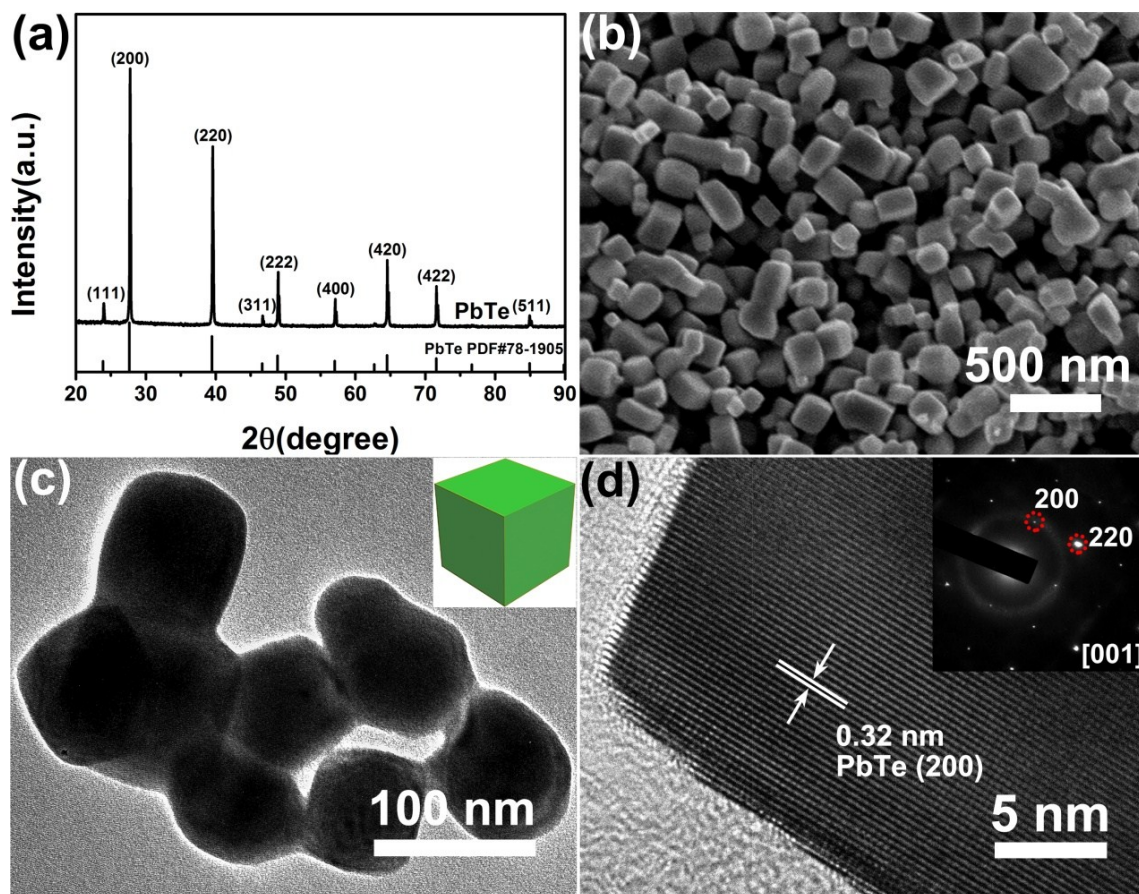
Figure S1. (a) X-ray powder diffraction pattern of the as-synthesized PbTe sample in comparison with the standard identification card of PbTe (JCPDS 78-1905), (b)FE-SEM image of pure PbTe nanocubes, (c) TEM micrograph of pure PbTe nanocubes with a size distribution estimates to range from 60 ~ 150 nm, (d) HRTEM image of PbTe nanocube, the inset shows selected area electron diffraction (SAED) of PbTe nanocubes, revealing a FCC structure.
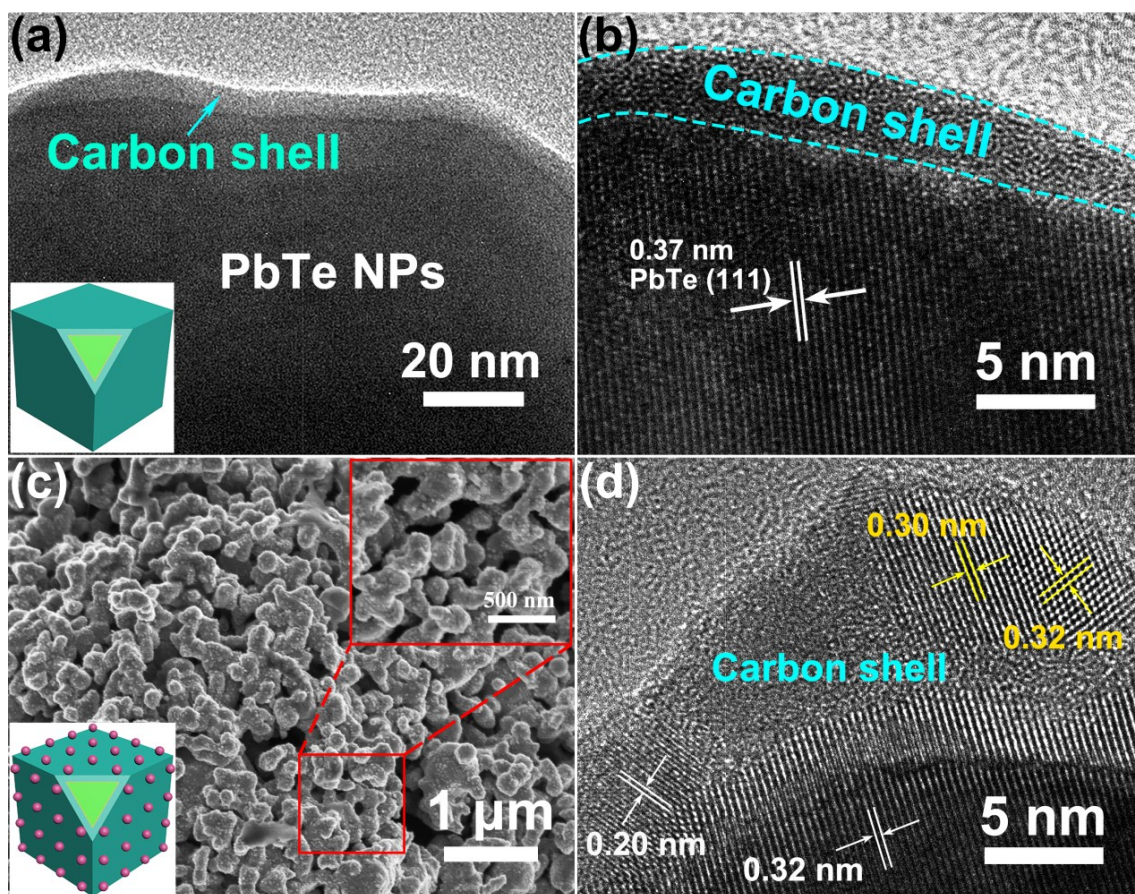
Figure S2. (a-b) Typical TEM images of PbTe@C core-shell nanostrucutures showing uniformly coated carbon shell on the PbTe core. The amorphous carbon shell are observed after H$_2$ annealing with the thickness around 2-5 nm, (c) FE-SEM image of annealed PbTe@C:Ag nanoparticles with inset clearly confirming the features of the Ag decorating, (d) HRTEM image of the PbTe/PbTe@C:Ag nanocomposites. The lattice spacing of ~0.323, 0.204, 0.298 and 0.317 nm corresponds to the (220) planes of PbTe, (220) planes of Ag, (-112) and (111) planes of Ag$_2$Te, respectively.
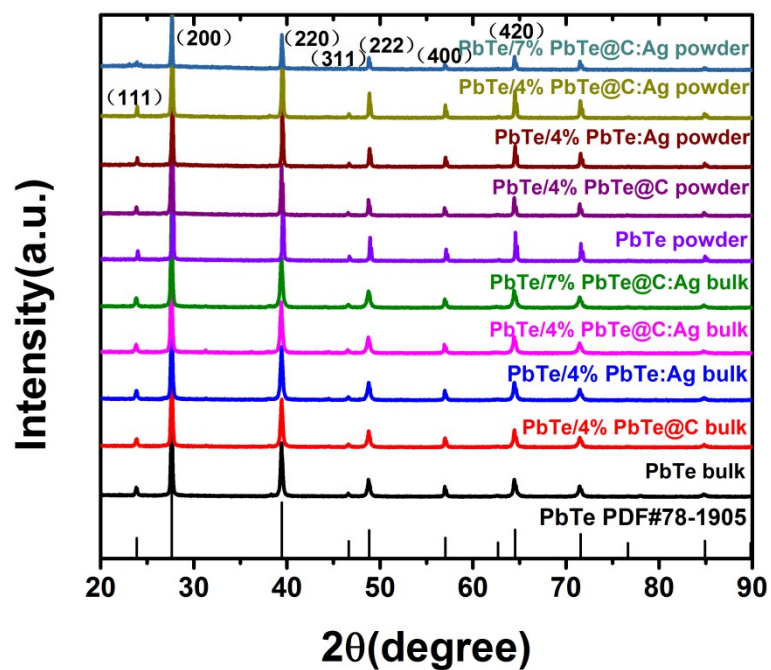
Figure S3. The XRD pattern for PbTe, PbTe/4%PbTe@C, PbTe/4%PbTe:Ag, PbTe/4% PbTe@C:Ag and PbTe/7% PbTe@C:Ag samples before and after SPS.
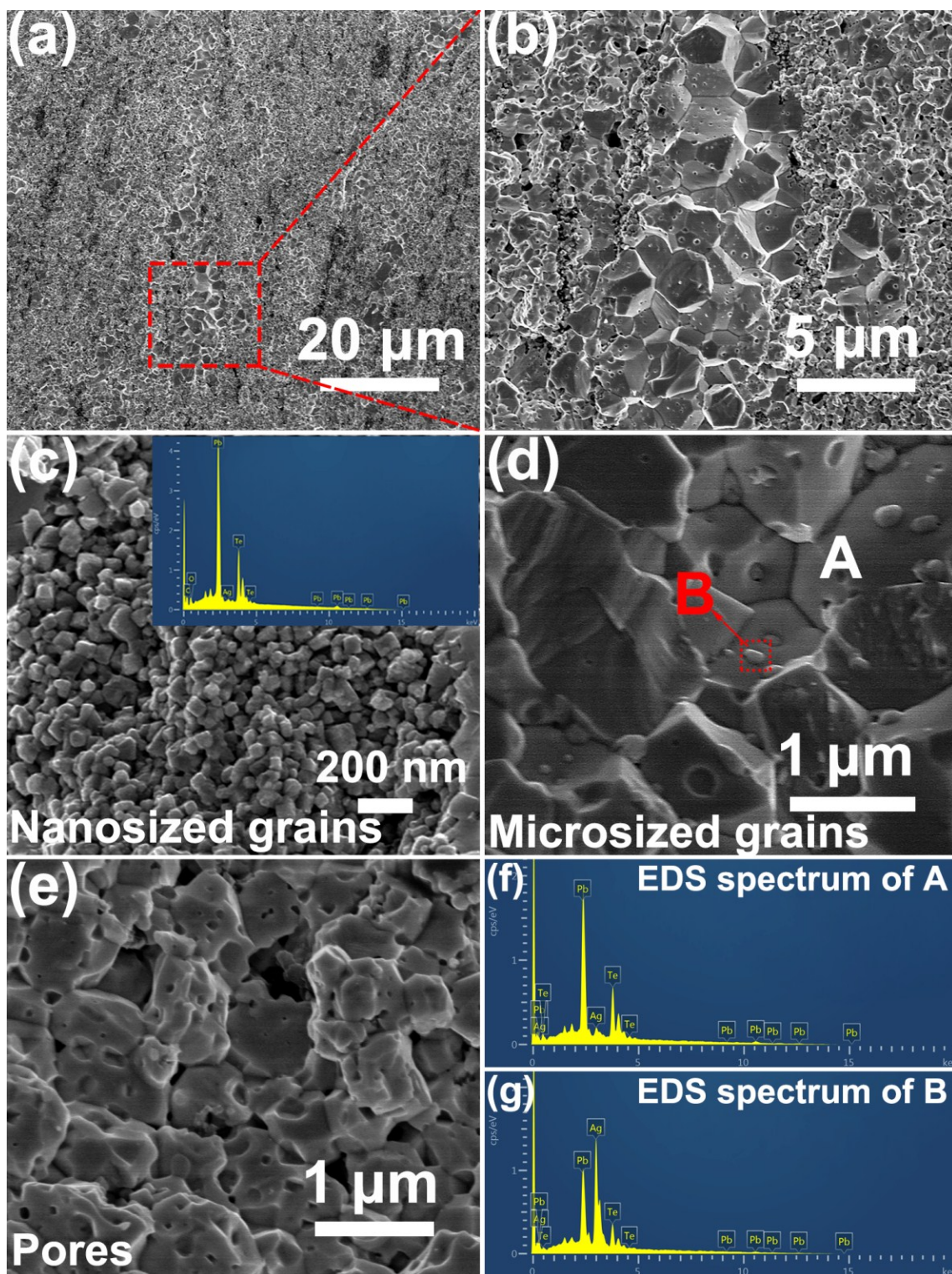
Figure S4. (a) FE-SEM image of the fractured surfaces of of PbTe/7%PbTe@C:Ag, (b) enlarged area marked in (a). FE-SEM image of (c) nanometer-sized zone, the inset shows the EDS spectrum of the nanometer-sized zone, (d) micrometer-sized zone, A and B represents the matrix and nano-precipitates, respectively. (e) pores of PbTe/7% PbTe@C:Ag. (f, g) EDS spectra of area A and B in (d), respectively.
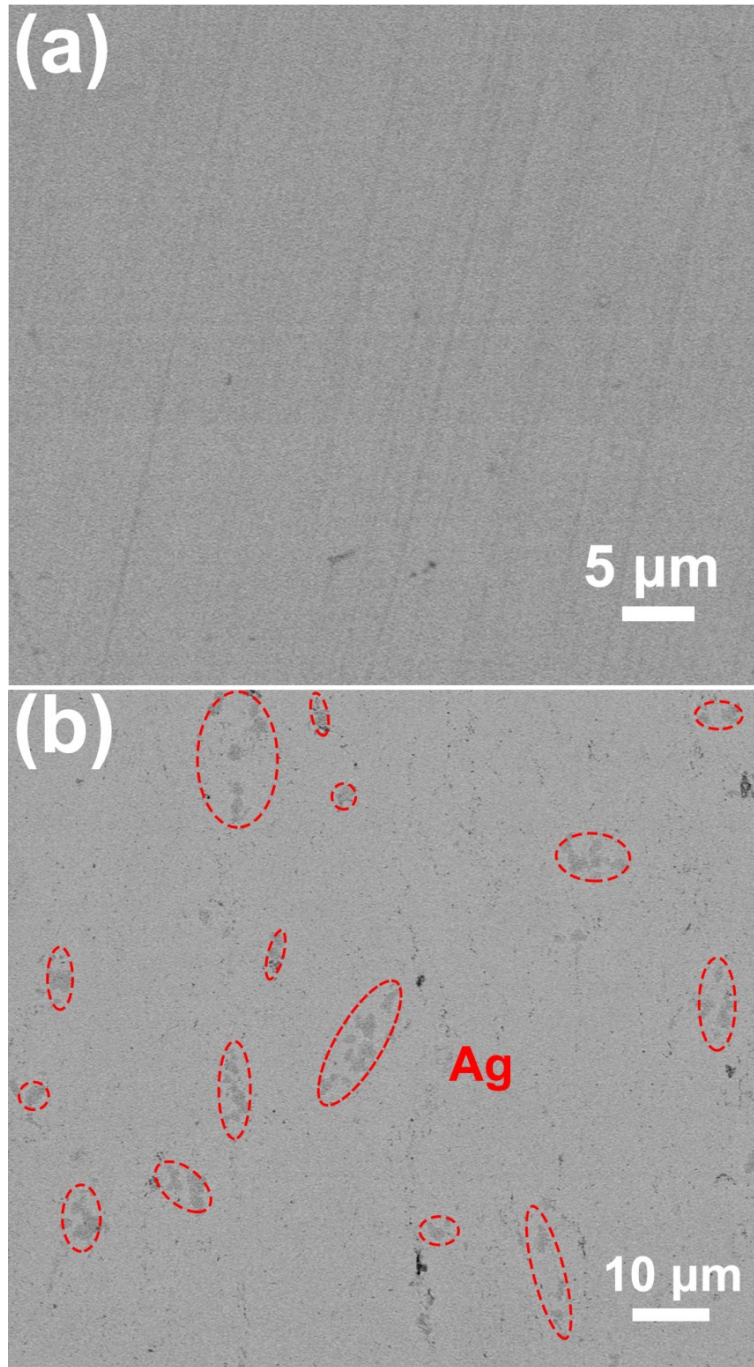
Figure S5. Back scattered electron images of polished surfaces: (a) pure PbTe and (b) PbTe/4%PbTe@C:Ag. In addition to the expected nanoscopic metallic Ag (dark island) embedded in the PbTe matrix phase(grey), pores is also observed (the black spots), which is consistent with the microstructure features.
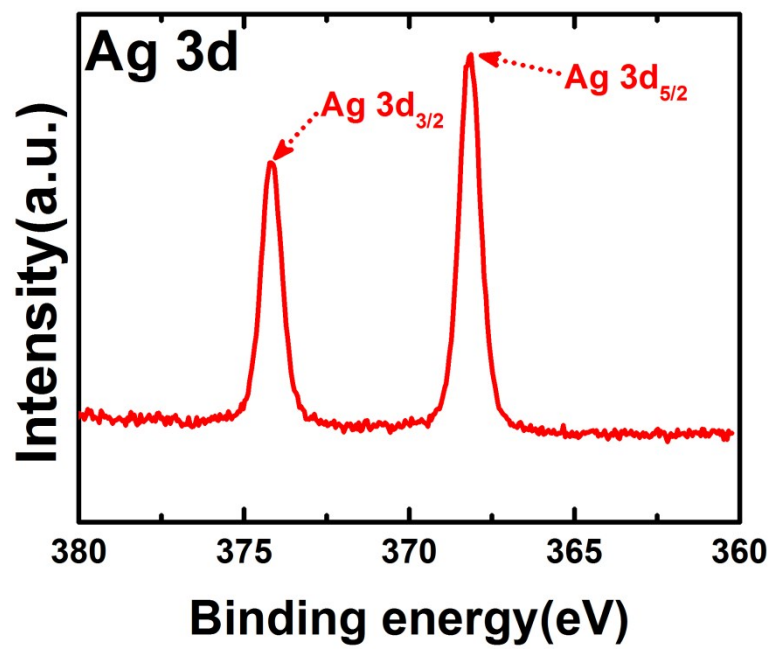
Figure S6. XPS spectra of Ag3d$_{3/2}$ and Ag3d$_{5/2}$ core state in PbTe/4%PbTe@C:Ag.
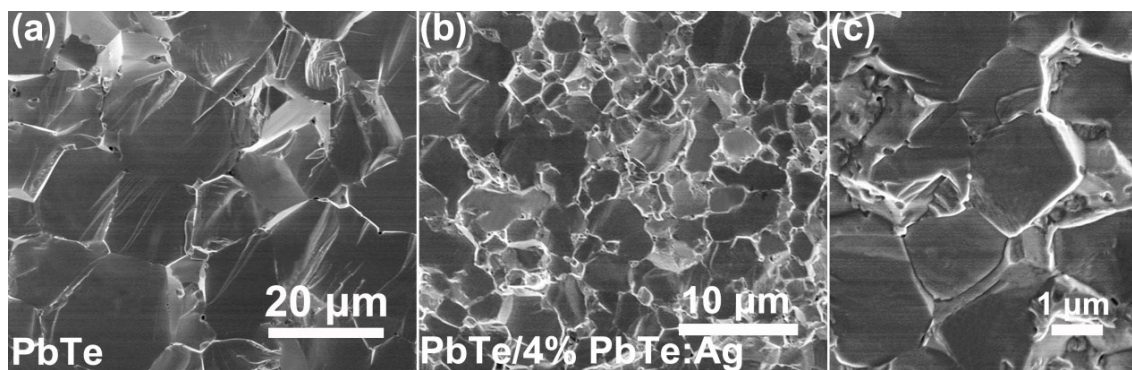
Figure S7. FE-SEM images of the fractured surfaces of (a) PbTe, (b) PbTe/4%PbTe:Ag. (c) High-magnification FE-SEM image of grains in PbTe/4%PbTe:Ag.
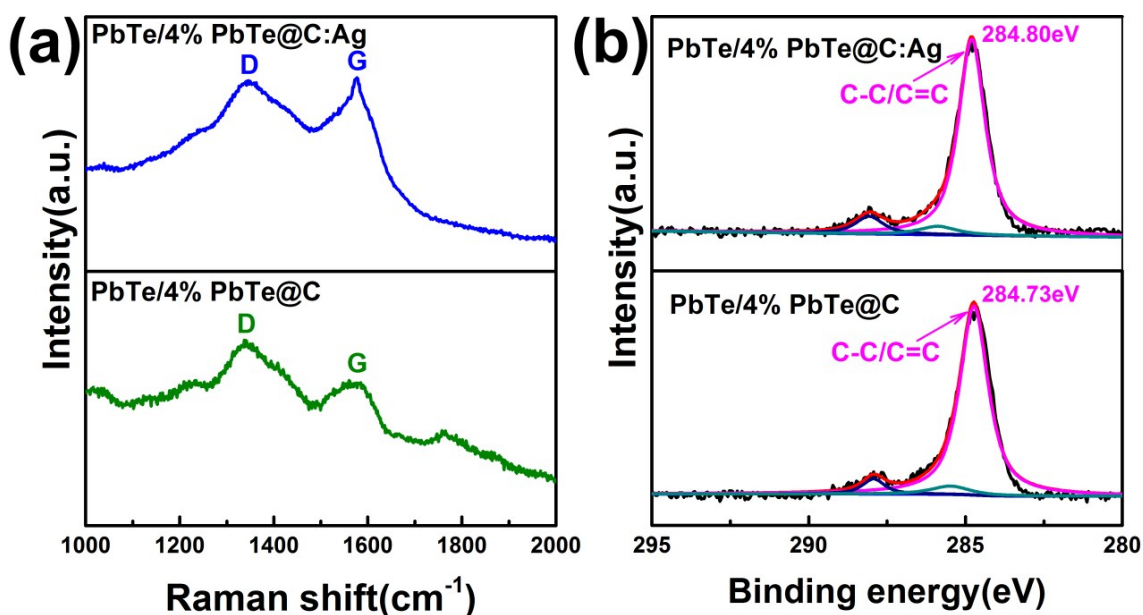
Figure S8. (a) Raman spectra of sintered bulks of the PbTe/4%PbTe@C and PbTe/4% PbTe@C:Ag. Both of the two Raman spectra exhibit two typical peaks of carbon at 1577 cm^{-1} (G-band) and at 1346 cm^{-1} (D-band) confirming the existence of carbon. (b) XPS spectra of C1s core state in sintered bulks of the PbTe/4%PbTe@C and PbTe/4%PbTe@C:Ag. The high-resolution C1s spectrum can be deconvoluted into three peaks and the binding energy of the C-C/C=C peaks are 284.73eV, 284.8eV for PbTe/4%PbTe@C and PbTe/4%PbTe@C:Ag, respectively. It is interesting to find that their binding energy of the C-C peak was higher than the standard C peak of 284.6 eV. Here we proposed that the high binding energy of our carbon-containing samples was due to the transfer of electrons from the carbon shell to the PbTe matrix.
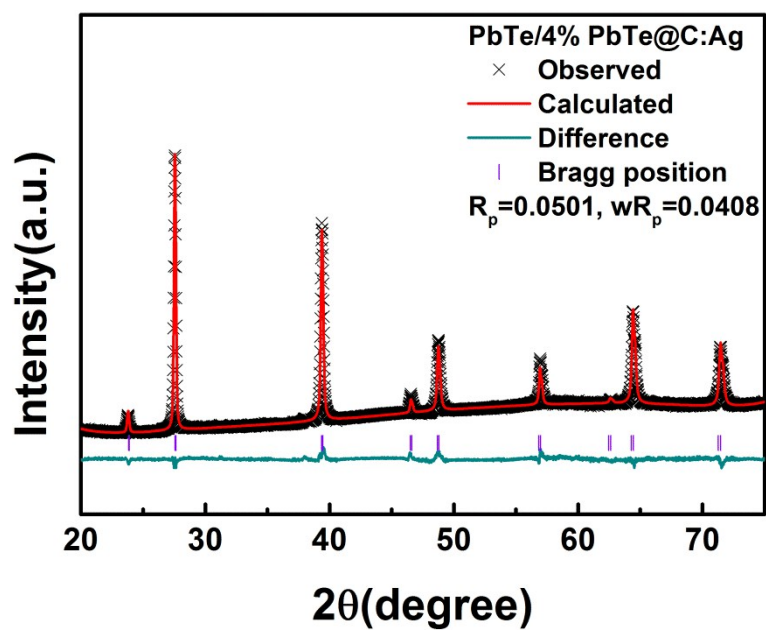
Figure S9. Representative Rietveld refinement result of PbTe/4%PbTe@C:Ag at 300K.
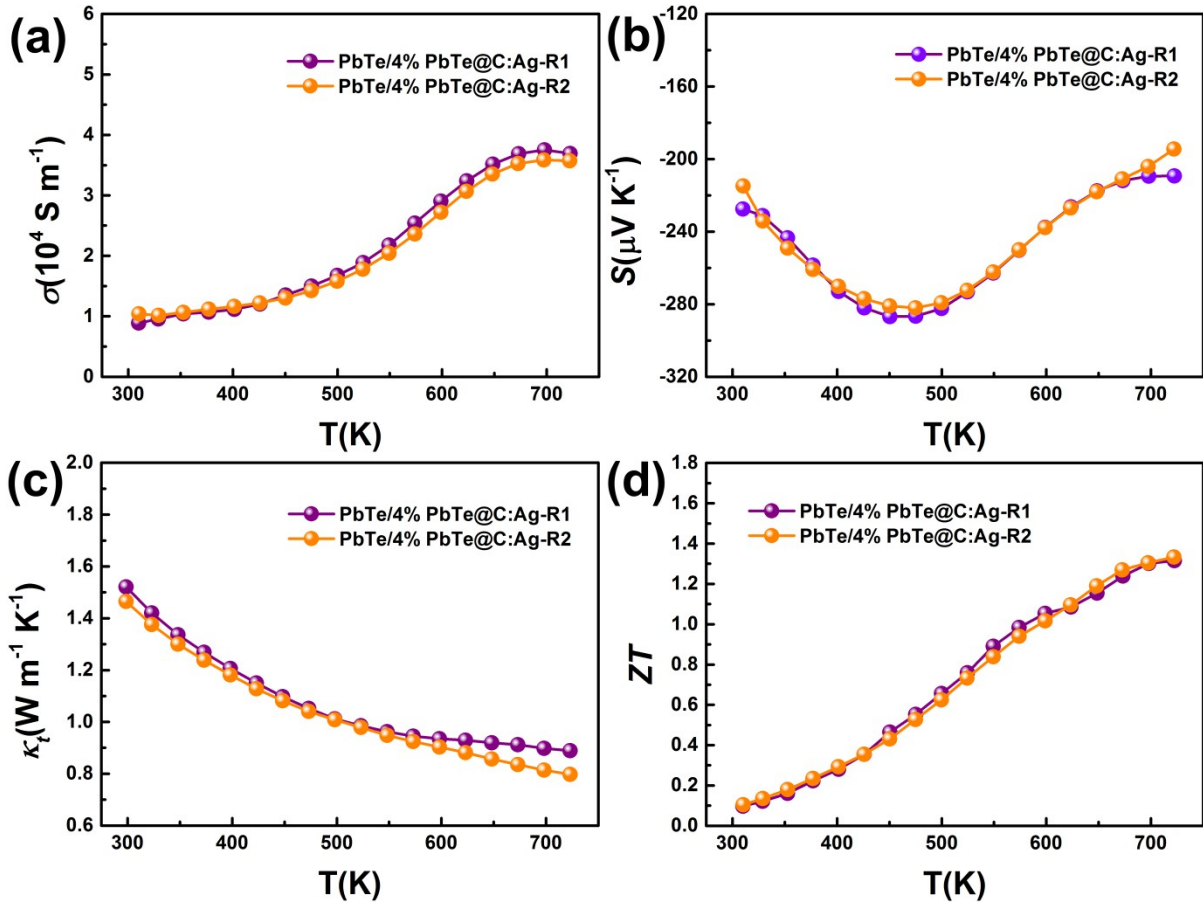
Figure S10. Temperature-dependent (a) electrical conductivity, (b) Seebeck coefficient, (c) total thermal conductivity, and (d) *ZT* for the reproduced PbTe/4%PbTe@C:Ag samples. Two samples were independently prepared and characterized. These results show high reproducibility of thermoelectric properties of PbTe/4%PbTe@C:Ag.
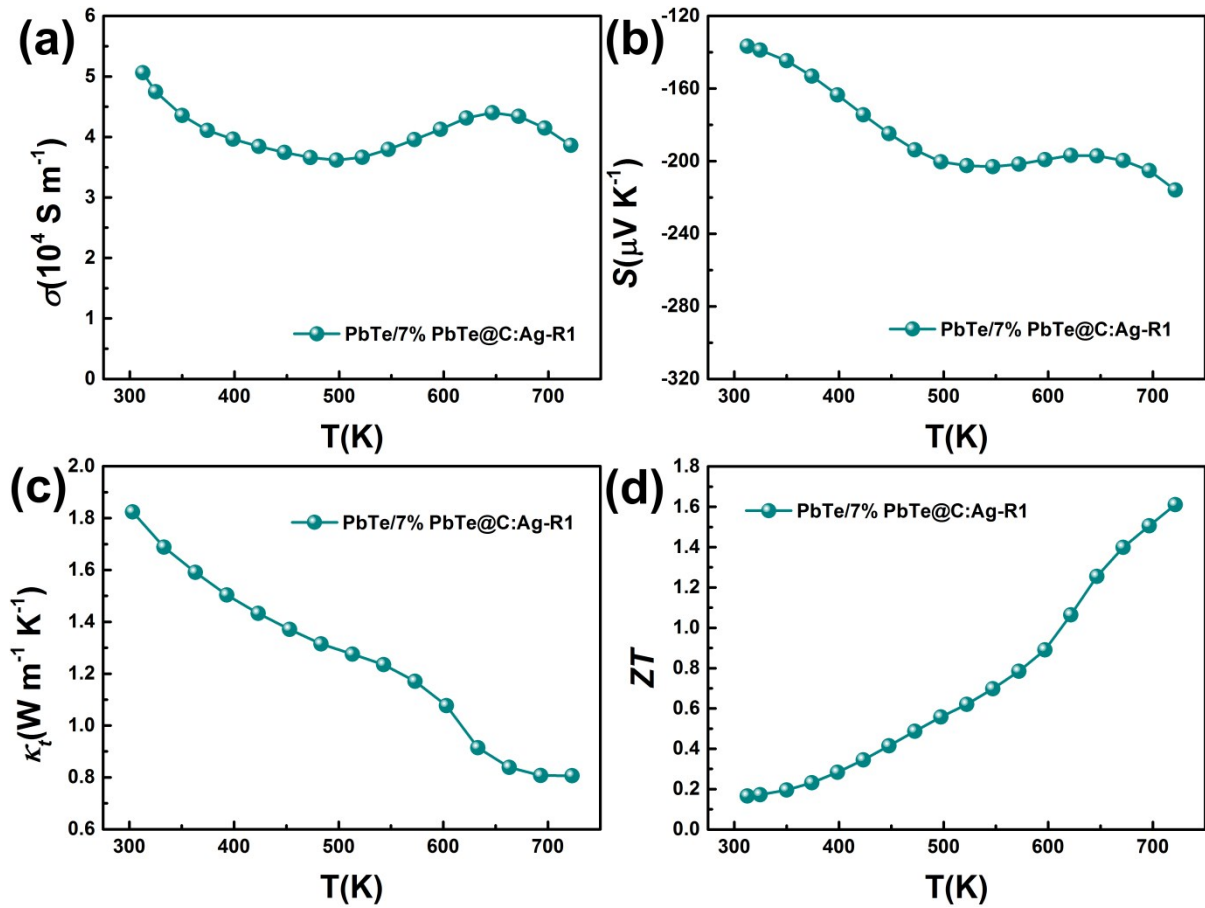
Figure S11. Temperature-dependent (a) electrical conductivity, (b) Seebeck coefficient, (c) total thermal conductivity, and (d) *ZT* for reproduced the PbTe/7%PbTe@C:Ag sample. The sample was independently prepared and characterized. These results show high reproducibility of thermoelectric properties of PbTe/7%PbTe@C:Ag.
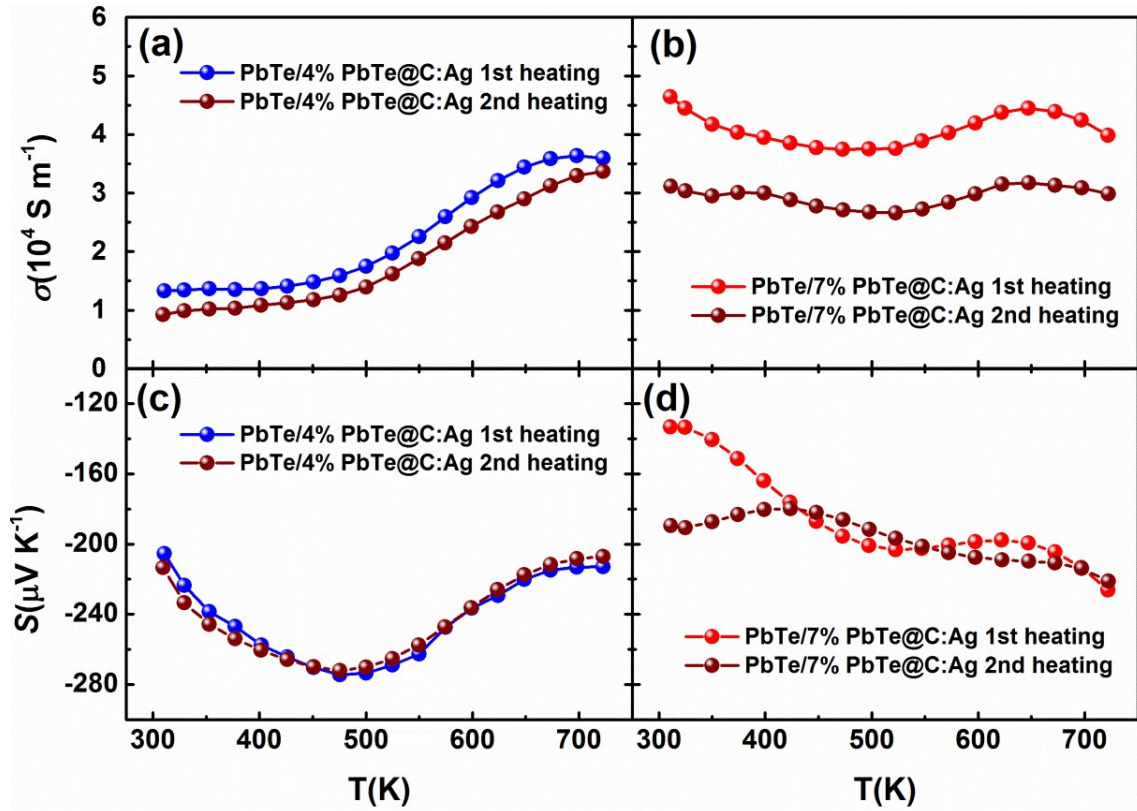
Figure S12. Temperature-dependent (a) electrical conductivity (b) Seebeck coefficient for PbTe/4%PbTe@C:Ag and PbTe/7%PbTe@C:Ag samples upon 1st and 2nd heating.
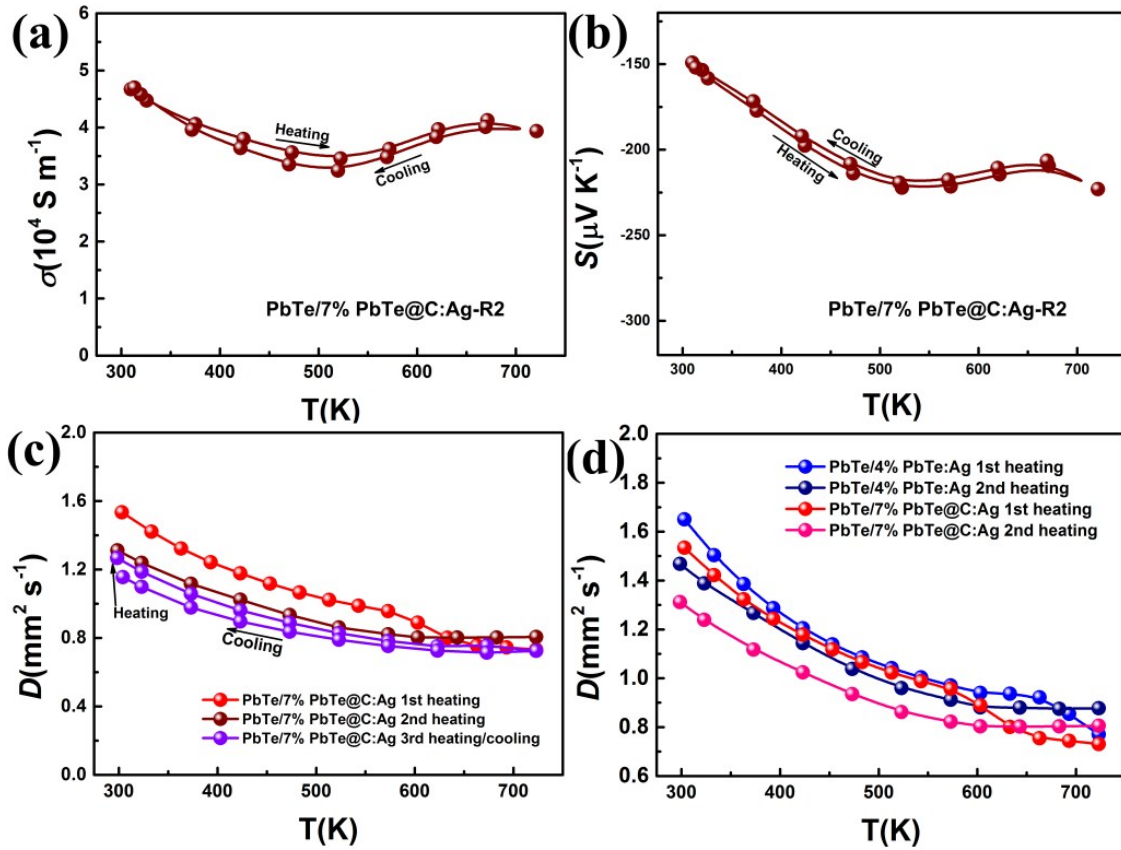
Figure S13. Temperature-dependent (a) electrical conductivity and (b) Seebeck coefficient for PbTe/7%PbTe@C:Ag-R2 upon heating and cooling. (c) temperature-dependent thermal diffusion coefficient for PbTe/7%PbTe@C:Ag sample upon 1st, 2nd heating and 3rd heating/cooling process and (d) temperature-dependent thermal diffusion coefficient for PbTe/4%PbTe:Ag and PbTe/7%PbTe@C:Ag samples upon 1st and 2nd heating process.
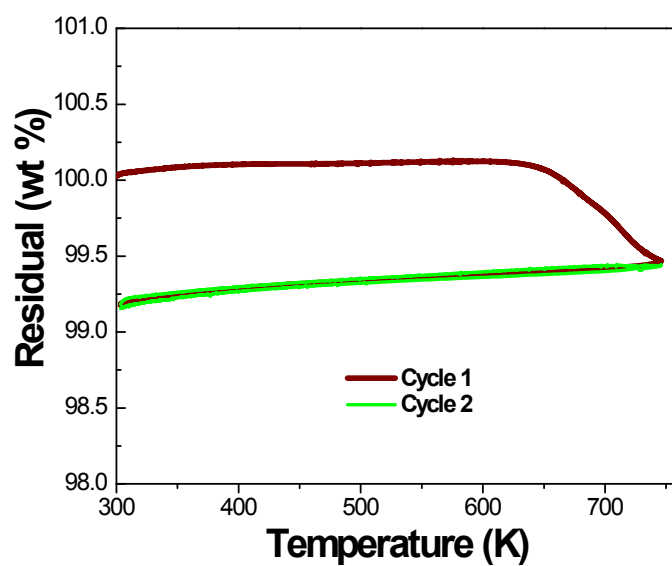
Figure S14. Thermogravimetric analysis on PbTe/7%PbTe@C:Ag in the 1st and 2nd heating and cooling process. It suggests that the sample become very stable after 1st heating and cooling cycle.

Table S1: Ag contents of the PbTe/4%PbTe@C:Ag (#1, #2) and PbTe/7%PbTe@C:Ag (#1, #2) samples tested by ICP-MS. Carbon contents of the PbTe/4%PbTe@C:Ag (#3) and PbTe/7%PbTe@C:Ag (#3) samples tested by high frequency infrared carbon/sulphur determinator. The fluctuation in Ag content might be due to the uniformly dispersion of Ag in the samples as indicated in Figure S5. So the average concentration was reasonably used. The mass content of Ag (%) in PbTe/4%PbTe@C:Ag and PbTe/7%PbTe@C:Ag is 0.48% and 0.86%, respectively.

Samples	Ag concentration (ng/g)	Sample concentration (mg/g)	Ag content (wt%)	C content (wt%)
PbTe/4%PbTe@C:Ag#1	26480	6.035	0.44	/
PbTe/4%PbTe@C:Ag#2	26480	5.040	0.52	/
PbTe/4%PbTe@C:Ag#3	/	/	/	0.35
PbTe/7%PbTe@C:Ag#1	9239	1.04	0.89	/
PbTe/7%PbTe@C:Ag#2	41200	5.225	0.83	/
PbTe/7%PbTe@C:Ag#3	/	/	/	0.52

Table S2. Density and electrical properties of the studied samples at room temperature.

Sample ID	n or p（10^{18} cm^{-3}）	μ（cm^2 V^{-1} s^{-1}）	Relative Density
PbTe	p=4.68	331.5	98.2%
PbTe/4%PbTe@C	n=1.39	229	91.0%
PbTe/4%PbTe:Ag	n=1.42	527.2	98.8%
PbTe/4%PbTe@C:Ag	n=2.65	313.2	91.6%
PbTe/7%PbTe@C:Ag	n=8.92	325.3	90.5%

Calculations

1. Calculation of Lorenz number

Because pure PbTe material shows a conductivity change from p-type to n-type due to the bipolar conductivity and a two valence band conduction mechanism in PbTe, the single parabolic band model was not suitable to calculated the Lorenz number.[1] Here, we used the equation:

$$L = 1.5 + exp\text{⟦?⟧} \ (\frac{-|S|}{116})$$

(1)

where L is in 10^{-8} W Ω K^{-2} and S in μV/K, as a satisfactory approximation for L.[2]

2. Calculation of temperature-dependent κ_l based on the modified Debye-Callaway model

Our SEM, HRTEM and STEM studies provided the quantitative information of defects generated in the samples. We calculated the temperature dependent κ_l using the modified Callaway-Debye model.[3, 4] We integrated various phonon scattering mechanisms, which were found in the local nanostructure samples by our microstructures studies. The κ_l is expressed as:

$$k_l = \frac{k_B}{2\pi^2 v_a} \left(\frac{k_B T}{\hbar}\right)^3 \int_0^{\frac{\theta_D}{T}} \tau_c \frac{e^x}{(e^x - 1)^2} x^4 dx$$

(2)

where x is defined as $\hbar\omega/k_B T$, k_B is the Boltzmann's constant, $\hbar$ is reduced Plank constant, v_a is an averaged phonon group velocity, T is absolute temperature and is Debye temperature. The τ_c is a combined term, which relates to many phonon scattering mechanisms. In this paper, the scattering from Umklapp process (τ_U), Normal process (τ_N), electron-phonon interaction (τ_E), Grain boundary scattering (τ_{GB}), pore scattering (τ_{Pore}), precipitates (τ_{NP}) , and point

defects (τ_{PD}) were considered, thus,

$$\tau_c^{-1} = \tau_U^{-1} + \tau_N^{-1} + \tau_E^{-1} + \tau_{GB}^{-1} + \tau_{Pore}^{-1} + \tau_P^{-1} + \tau_{PD}^{-1}$$

(3)

The first three contributions originate mainly from the matrix. It should be pointed out that among all the parameters used to calculated the temperature dependent κ_l of the PbTe (U+N) and PbTe/4% PbTe@C:Ag (U+N+E+GB+Pore+P+PD) based on the Callaway's model, there is one fitting parameter, ratio of normal phonon scattering to Umklapp scattering, β. We obtained the ratio of normal phonon scattering to Umklapp scattering, β, by fit the lattice thermal conductivity of PbTe sample using the U+N+E processes based on Callaway's model. The value of β in this work is 3.3, which is close to the reported one, 2.9, used for n-type PbTe materials. We figured out the temperature dependent amount of dissolved Ag (x). For convenience, we assumed that the number density of nanoscale precipitates is proportion to the amount of Ag nano-precipitates in all the temperature range.[5] By using the results of temperature dependent x and V_P, we calculated the theoretical κ_l in temperature range of 300K~723K.

Table S3. Relaxation times for different scatter mechanisms. Equations for relaxation times for Umklapp process (τ_U), Normal process (τ_N), electron-phonon interaction (τ_E), Grain boundary scattering (τ_{GB}), pore scattering (τ_{Pore}), precipitates (τ_P) and point defects (τ_{PD}).

Types of scattering mechanisms	Relaxation times($\tau(s^{-1})$)
Umklapp processes	$$\tau_U^{-1} = \frac{\hbar\gamma^2}{Mv_a^2\theta_D}\omega^2 T exp\left(-\theta_D/3T\right)$$
Normal processes	$$\tau_N^{-1} = \beta\tau_U^{-1}$$
Electron-phonon interaction	$$\tau_E^{-1} = \frac{E_{def}^2 m^{*2}\omega}{2\pi\hbar^3\rho v_a}$$
Grain boundaries	$$\tau_{GB}^{-1} = v_a/D_{grain}$$
Pore structures	$$\tau_{Pore}^{-1} = \frac{P}{2}\tau_{bulk}^{-1} + \frac{3Pv_a}{2D_{pore}}$$
Precipitates	$$\tau_P^{-1} = v_a\left(\sigma_s^{-1} + \sigma_l^{-1}\right)^{-1}V_P$$
Point defects	$$\tau_{PD}^{-1} = \frac{\overline{V}\omega^4}{4\pi v_a^3}\sum_i x_i\left[\left(\frac{M_i - M}{M}\right)^2 + \varepsilon\left(\frac{a_i - a}{a}\right)^2\right]$$

Table S4. Input parameters for calculation of relaxation time of phonon scattering

Parameters	Description	Values	Ref.
γ	Gruneisen parameter	1.96	[5]
v_L	Longitudinal sound velocity	2919 m s^{-1}	[5]
v_T	Transversal sound velocity	1620 m s^{-1}	[5]
v_a	Average sound velocity	1805 m s^{-1}	[5]
θ_D	Debye temperature	136 K	[5]
$\bar{M}$	Average mass of an atom	2.78 *10^{-25} Kg	This work
v_p	Poisson ratio	0.28	This work
β	Ratio of Normal phonon scattering to Umklapp scattering	3.3	This work, fitted
E_{def}	Acoustic phonon deformation potential	22 eV	[6]
m^*	Effective mass of charge carrier	0.23 m$_e$	[6]
ρ	Sample density	7.55 g cm^{-3}	This work
D_{grain}	Average grain diameter	500 nm	This work
P	Porosity	8 %	This work
D_{pore}	Average pore diameter	100 nm	This work
R	Average radius of nanoscale precipitates	5 nm	This work
D_{PbTe}	Mass density of PbTe	8.24 g cm^{-3}	--
D_{Ag}	Mass density of Ag	10.5 g cm^{-3}	--
V_P	Number density of nanoscale precipitates	2*10^{12} cm^{-2}	This work
x_i	Impurities concentration in solid solutions	i$_{Ag}$=0.01	This work
M_i	Atom mass of impurity	107.87 g mol^{-1}	--
M	Atom mass of matrix	334.8 g mol^{-1}	--
ε	Anharmonic parameter	110	This work
a_i	Lattice parameters for Pb$_{0.99}$Ag$_{0.01}$Te	6.464 Å	This work

[1] L. Yang, Z.-G. Chen, M. Hong, L. Wang, D. Kong, L. Huang, G. Han, Y. Zou, M. Dargusch, J. Zou, n-type Bi-doped PbTe Nanocubes with Enhanced Thermoelectric Performance, Nano Energy 2017, 31, 105.

[2] H.-S. Kim, Z. M. Gibbs, Y. Tang, H. Wang, G. J. Snyder, Characterization of Lorenz number with Seebeck coefficient measurement, APL Materials 2015, 3, 041506.

[3] J. He, J. Androulakis, M. G. Kanatzidis, V. P. Dravid, Seeing is believing: weak phonon scattering from nanostructures in alkali metal-doped lead telluride, Nano Lett 2012, 12, 343.

[4] J. Callaway, Model for Lattice Thermal Conductivity at Low Temperatures, Physical Review 1959, 113, 1046.

[5] L. Fu, M. Yin, D. Wu, W. Li, D. Feng, L. Huang, J. He, Large enhancement of thermoelectric properties in n-type PbTe via dual-site point defects, Energy & Environmental Science 2017, 10, 2030.

[6] Y. Pei, H. Wang, G. J. Snyder, Band engineering of thermoelectric materials, Adv Mater 2012, 24, 6125.